Journal of Biomechanics

Validation of Markerless Strain-Field Optical Tracking Approach for Soft Tissue Mechanical Assessment

--Manuscript Draft--

Manuscript Number:	BM-D-19-01235R2
Article Type:	Full Length Article (max 3500 words)
Keywords:	Strain field; tensile test; Demons
Corresponding Author:	Mark David Olchanyi, BEng Imperial College London London, UNITED KINGDOM
First Author:	Mark David Olchanyi
Order of Authors:	Mark David Olchanyi
	Amir Sadikov
	Jennifer Frattolin
	Sumesh Sasidharan
	M Yousuf Salmasi
	Lowell T. Edgar
	Omar Jarral
	Thanos Athanasiou
	James E. Moore
Abstract:	Strain measurement during tissue deformation is crucial to elucidate relationships between mechanical loading and functional changes in biological tissues. When combined with specified loading conditions, assessment of strain fields can be used to craft models that accurately represent the mechanical behavior of soft tissue. Inhomogeneities in strain fields may be indicative of normal or pathological inhomogeneities in mechanical properties. In this study, we present the validation of a modified Demons registration algorithm for non-contact, marker-less strain measurement of tissue undergoing uniaxial loading. We validate the algorithm on a synthetic dataset composed of artificial deformation fields applied to a speckle image, as well as images of aortic sections of varying perceptual quality. Initial results indicate that Demons outperforms recent Optical Flow and Digital Image Correlation methods in terms of accuracy and robustness to low image quality, with similar runtimes. Demons achieves at least 8% lower maximal deviation from ground truth on 50% biaxial and shear strain applied to aortic images. To illustrate utility, we quantified strain fields of multiple human aortic specimens undergoing uniaxial tensile testing, noting the formation of strain concentrations in areas of rupture. The modified Demons algorithm captured a large range of strains (up to 50%) and provided spatially resolved strain fields that could be useful in the assessment of soft tissue pathologies.

Cover Letter

We hereby declare that there is no duplicate publication elsewhere of any part of this work. There are no commercial relationships which might lead to a conflict of interests. The typescript has been read and agreed by all authors.

We hereby declare that all authors were fully involved in the study and preparation of the manuscript and the material within has not been and will not be submitted for publication elsewhere.

Authors:

Mark D. Olchanyi

Amir Sadikov

Jennifer Frattolin

Sumesh Sasidharan

M Yousuf Salmasi

Lowell T. Edgar

Omar Jarral

Thanos Athanasiou

James E. Moore Jr

Corresponding author:

Mark D. Olchanyi

olchanyi@mit.edu

mark.olchanyi16@imperial.ac.uk

Imperial College London, Department of Bioengineering

London, UK

Response to Reviewers

The authors would like to thank the editor and reviewers for their time and efforts. The valuable comments have helped us improve the manuscript.

The original comments from the reviewers are shown in italics, with the corresponding response from the authors provided directly below in red.

Reviewer #1 (Remarks to the Author):

1. *Title: "… Soft Tissue Mechanical Assessment" is suggested to be replaced with a more specific description "… Aortic Strain Assessment"*

   We prefer to keep the title as is, because we are confident that this technique can be used for a wide variety of soft tissues. Making the title more specific could unnecessarily limit the target audience. Instead, we have clarified in the Abstract that we have only tested on aortic specimens and have edited the Discussion to clarify that the technique has the potential for application to other tissues and imaging techniques.

2. *Abstract seems no specific results and conclusions, please add them.*

   We have added results and a concluding sentence to the abstract.

3. *Line 21: DIC show be replaced with digital image correlation.*
4. *All the definition of abbreviations should be checked (they should be only defined at first appearance from Introduction to Conclusion, please do not define repeatly (sic), e.g. Line 144 MSE; Line 160 SNRS, …)*
5. *Line 176: "4°C" should be "4 °C"*
6. *Line 177: "20 mm x 5 mm" should be "20 mm × 5 mm" (the multiplication character is different from English alphabet x)*
7. *Line 183: "0.01N" should be "0.01 N"*
8. *Line 195: "50mm" should be "50-mm"*
9. *Line 197: "15cm" should be "15 cm"*
10. *Line 204: "28.005s" should be "28.005 s", "450x450" should be "450 × 450"*
11. *Line 243: "29dB" should be "29 dB"*
12. *Line 244: "310 x 310" should be "310 × 310"*

    We apologize for these mistakes. These have been corrected.

13. *The font in all figures should be the same or close, e.g. in Figure 2 & 4, "A" and "B" look much larger than "C" and "D".*
14. *Figure 4: In figure legend, the format of "A", "B", … is different from those in other figures, e.g. (A)*

    We apologize for the formatting errors. These have been corrected.

15. *Figure 6: I think it should be better to identify tissue rupture combined with force changes, because the identification with background relies on sample thickness and transactional structure changes (the background may be still absent even rupture happens)*

We have edited the legends of Figure 6 and 7 that the green arrow indicates “visible evidence of rupture”. We have also clarified that we did in fact use the force curves, not visual cues, to determine when rupture happened.

16. *Figure 7: Please also show x-y axis in Figure 1A-right, and check the description of the first sentence of Figure 7 legend (it is hard to read).*

    The first sentence has now been edited for more clarity.

Other minor edits were made.

Validation of Markerless Strain-Field Optical Tracking Approach for Soft Tissue Mechanical Assessment

Mark D. Olchanyi[a*], Amir Sadikov[a*], Jennifer Frattolin[a], Sumesh Sasidharan[a], M Yousuf Salmasi[b], Lowell T. Edgar[c], Omar Jarral[b], Thanos Athanasiou[b], James E. Moore Jr.[a]

[a]*Department of Bioengineering, Imperial College London, London, UK, SW7 2AZ*

[b]*Department of Surgery and Cancer, Imperial College London, London, UK, SW7 2AZ*

[c]*Usher Institute, The University of Edinburgh Medical School, UK, EH16 4SB*

ABSTRACT

Strain measurement during tissue deformation is crucial to elucidate relationships between mechanical loading and functional changes in biological tissues. When combined with specified loading conditions, assessment of strain fields can be used to craft models that accurately represent the mechanical behavior of soft tissue. Inhomogeneities in strain fields may be indicative of normal or pathological inhomogeneities in mechanical properties. In this study, we present the validation of a modified Demons registration algorithm for non-contact, marker-less strain measurement of tissue undergoing uniaxial loading. We validate the algorithm on a synthetic dataset composed of artificial deformation fields applied to a speckle image, as well as images of aortic sections of varying perceptual quality. Initial results indicate that Demons outperforms recent Optical Flow and Digital Image Correlation methods in terms of accuracy and robustness to low image quality, with similar runtimes. Demons achieves at least 8% lower maximal deviation from ground truth on 50% biaxial and shear strain applied to aortic images. To illustrate utility, we quantified strain fields of multiple human aortic specimens undergoing uniaxial tensile testing, noting the formation of strain concentrations in areas of rupture. The modified Demons algorithm captured a large range of strains (up to 50%) and provided spatially resolved strain fields that could be useful in the assessment of soft tissue pathologies.

Key words: Strain field, Tensile test, Demons

Abstract Word Count: 215

Total Word Count (Intro-Discussion): 3456

INTRODUCTION

Knowledge of the mechanical properties of soft tissues, such as the aorta, is essential in understanding pathological and physiological behaviors and the effects of different disease states, treatments, and pharmacological agents. This characterization can aid in predicting or diagnosing cardiovascular diseases (Vorp, 2007). Due to its non-homogeneity, anisotropy, and ability to undergo finite deformations, complex constitutive laws are required to model soft tissue mechanical behavior (Chen, Zhao, Lu, & Kassab, 2013) (Khanafer, et al., 2011). Estimation of model parameters requires high-fidelity strain measurements to ensure accurate tissue characterization (Watton & Hill, 2007).

There have been numerous algorithms developed for biomedical non-rigid registration, the most notable of which are Optical Flow (OF) and Digital Image Correlation (DIC). OF is one of the most widely used registration algorithms for local motion estimation and strain field calculation. However, OF assumes brightness constancy, which leads to poor accuracy in varied lighting. In addition, most OF variants suffer from accuracy losses in frame differencing, which depend highly on local feature speeds. DIC has emerged as a standard technique for soft tissue mechanical assessment. However, since DIC is reliant upon cross-correlation to determine shifts between images, the application of markers (Choudhury, et al., 2009) (Huang, Korhonen, Turunen, & Finnila, 2019) or textured surface finishes (Barranger, Doumalin, Dupré, & Germaneau, 2010) is necessary to provide sufficient contrast to correlate images well without phase ambiguity. Most soft tissues lack sufficient texture for DIC to be robust without surface preparation (Palanca, Tozzi, & Cristofolini, 2016). Attaching markers can modify material properties and may suffer from unreliable adherence to wet tissues.

In this study, we have investigated non-rigid registration techniques to overcome these issues. One popular class of algorithms for non-rigid registration is the Demons algorithm, which models the matching of two images as a diffusion process (Thirion, 1998). Further work has constrained the optimization scheme in Thirions Demons to only diffeomorphic mappings (Vercauteren, Pennec, Perchant, & Ayache, 2009) by providing a lie pseudo-group structure on the space of diffeomorphisms. This mathematical reformulation allows the displacement field to be efficiently calculated by the fast vector exponential of the flow field and converges to smooth, invertible transformations (Bossa, Zacur, & Olmos, 2008). Diffeomorphic Demons could therefore provide a promising framework for the estimation of strain fields of biological surfaces.

The goal of this study is to modify and apply an existing non-parametric image registration algorithm to calculate the marker-less deformation of soft biological tissues. We propose a modified Diffeomorphic Demons registration and strain tracking algorithm to compute two-dimensional strain fields from uniaxial tensile tests of aortic tissue using only the natural optical features of the tissue. We validate the modified Demons algorithm by measuring the convergence of the calculated strain field to a predefined strain field of an artificial dataset, created by applying linear biaxial as well as shear strain to a speckled image. We then compare the robustness of the modified Demons algorithms to standard DIC and OF algorithms on images of aortic aneurysm samples with varying surface quality (the number of discernable structures and grain boundaries, as well as the amount of texture). We also investigate the effects of downsampling and white noise injection on the performance of the Demons, DIC, and OF algorithms. Lastly, we use the modified Diffeomorphic Demons algorithm to measure the deformation of human aortic aneurysm specimens undergoing tensile testing. Hereafter, we refer to the modified Diffeomorphic Demons algorithm simply as “Demons”.

2. MATERIALS AND METHODS

2.1 Demons Strain Tracking Algorithm and Validation Testing

Demons registration and strain tracking algorithm is proposed to compute two-dimensional strain fields from images acquired during uniaxial tensile tests of aortic aneurysm samples, using only the native optical features of the tissue. The strain fields are determined by Demons according to the protocol below:

I. Images are acquired during tensile testing at a frequency of 0.1 Hz. To better illuminate the sample, a near-UV LED light (395 nm, 20 W, 1200 lumens) is used, with blackout screens surrounding the testing chamber to block ambient light. After testing, the images are converted into 16-bit greyscale format and histogram intensities of each image pair are matched to account for LED flicker.

II. Demons (Cahill, Noble, & Hawkes, 2009) (Verauteren, Pennec, Perchant, & Ayache, 2009) is used to register the second (moving) image in the pair to the first (fixed) image (Thirion, 1998). The loss function implemented across each iteration is the Mean Square Error (MSE) of the intensity fields. This is calculated between the warped fixed image and moving image, without a regularization term, which is typically the gradient norm of the transformation. A sufficiently smooth displacement field is instead achieved by iterative Gaussian filtering of each step update to the flow fields. This results in a simpler loss function that is in most cases easier to solve, while still providing stable solutions. A Gradient Descent with Warm Restarts (GDR) solver is implemented (Loshchilov & Hutter, 2017) to optimize the loss function. Warm restarts are achieved by momentarily increasing the learning rate if the loss function was either steadily increasing or stalling.

Usually a Gauss-Newton solver is used, however, its performance noticeably deteriorates as the number of variables increases, due to the ill-posed approximation of the Hessian. Gradient

Descent (GD) methods offer a simple, computationally efficient way of minimizing the loss function, with nearly global convergence properties under mild conditions. Furthermore, with warm restarts, GD methods can escape non-optimal submanifolds (Chizat & Bach, 2018).

In this study, a configuration of 4 pyramid levels, with up to 5000 iterations and 8 restarts per level, and an accumulated field smoothing parameter of 3.0 were used. These hyperparameters were increased to the point of diminishing returns in terms of algorithm performance. In general, more pyramid levels, iterations, and restarts lead to higher accuracy, but longer computational time. A larger smoothing parameter provides greater regularization.

III. For an image sequence (more than two images), the image pixels are iteratively tracked and updated via the calculated displacement fields, generated for each k^{th} frame, showing the x and y distance each pixel moves from the k^{th} frame to the $(k+1)^{th}$ frame. If the effect of the pixels moving is not considered, the displacements will be erroneously attributed to pixels further afield. Therefore, a total displacement field is generated, which tracks the x and y distance each pixel travels from the 1^{st} frame to the $(k+1)^{th}$ frame. It is calculated by iteratively warping the total displacement field with the displacement field of the k^{th} frame to update locations. Warping is executed via inverse mapping, which modifies the spatial coordinates of each input pixel via the displacement field found by Demons, followed by bicubic interpolation to determine the output pixel value.

IV. A triangular mesh grid is generated from equidistant points with stride lengths of 5 pixels along the image. This mesh size is changed programmatically for each trial to ensure accurate performance. In general, smaller elements are prone to noise, but larger elements do not sufficiently characterize the strain heterogeneity. Triangulation of the mesh is optimized using the Delaunay method, which maximizes the minimum angle of all angles of the triangular mesh elements. The triangulation implementation is based on a variant of the Quickhull algorithm

(Barber, Dobkin, & Huhdanpaa, 1996), which regularizes the grid, simplifying indexing of strain elements.

V. Each mesh element in the moving image is matched with its homologous element in the fixed image to calculate the two-dimensional Green-Lagrange strain tensor, $\boldsymbol{E}$ (Hiorns, et al., 2016).

$$\boldsymbol{E} = \frac{1}{2}[(\nabla_{\mathbb{X}}\boldsymbol{u})^T + \nabla_{\mathbb{X}}\boldsymbol{u} + (\nabla_{\mathbb{X}}\boldsymbol{u})^T \cdot \nabla_{\mathbb{X}}\boldsymbol{u}]$$

Where $\nabla_{\mathbb{X}}\boldsymbol{u}$ is the gradient displacement tensor.

In 2D:

$$\boldsymbol{E} = \begin{bmatrix} \boldsymbol{E_{xx}} & \boldsymbol{E_{xy}} \\ \boldsymbol{E_{xy}} & \boldsymbol{E_{yy}} \end{bmatrix}$$

$$\boldsymbol{E_{xx}} = \frac{\partial u}{\partial X} + \frac{1}{2}\left[\left(\frac{\partial u}{\partial X}\right)^2 + \left(\frac{\partial v}{\partial X}\right)^2\right]$$

$$\boldsymbol{E_{yy}} = \frac{\partial v}{\partial Y} + \frac{1}{2}\left[\left(\frac{\partial u}{\partial Y}\right)^2 + \left(\frac{\partial v}{\partial Y}\right)^2\right]$$

$$\boldsymbol{E_{xy}} = \frac{1}{2}\left(\frac{\partial v}{\partial Y} + \frac{\partial u}{\partial X}\right) + \frac{1}{2}\left[\left(\frac{\partial u}{\partial X}\frac{\partial u}{\partial Y}\right) + \left(\frac{\partial v}{\partial X}\frac{\partial v}{\partial Y}\right)\right]$$

The strain-tracking pipeline outputs a frame-by-frame analysis of x-strain, y-strain, and shear strain magnitudes, including a contour map of strain elements for each Green-Lagrange strain component (Olufsen & Andersen, 2019).

To validate the Demons algorithm, predefined strain fields of biaxial and shear strains of up to 50% were applied to a 450x450 speckled image. The strain fields of the speckled image were calculated by Demons, and the convergence of the calculated strain field was compared to the predefined strain field of the artificial datasets. Maximal deviations, maximal standard deviation, and Pearson's Correlation coefficients were recorded for the biaxial and shear strain dataset (Table 1). Maximal deviations were calculated as the absolute difference between the predefined mean strain and mean strain given by Demons. Maximal standard deviation was defined in the spatial sense. The Pearson's Correlation Coefficient served as an additional accuracy metric for the algorithm validation. The effects of noise injection and downsampling were also assessed at 5% biaxial strain, with respect to the MSE. Downsampling was achieved via bicubic interpolation. Signal-to-noise ratios (SNRs) between 10 and 30 dBs and downsampling factors between 0.2 and 1 were considered.

2.2 Validation Testing with DIC and OF Methods

Methods from the Python library μDIC (Olufsen & Andersen, 2019) (Brox, Bregler, & Malik, 2009) were implemented to induce artificial deformations of up to 50% biaxial strain on two sample aortic tissue images, which had differing image quality with respect to the natural optical features for tracking. The image pair was chosen to assess the effect of image quality, measured by Perception Based Image Quality Evaluator (PIQE) scores, on the performance of Demons. To evaluate image quality, PIQE scores were measured. For comparison testing, standard OF and DIC methods were implemented. The OF method uses Large Displacement Optical Flow (LDOF), a variational course-to-fine algorithm that includes correspondences from sparse feature matching (Brox, Bregler, & Malik, 2009). The DIC method used (from the μDIC library) is a global DIC algorithm with a modified Newton-Raphson optimization scheme and B-spline discretization of deformation fields. The calculated strain field determined by Demons, OF, and DIC methods were compared for the artificial dataset. In addition, maximal deviations, maximal standard deviations, and Pearson's Correlation Coefficients were recorded for both images for Demons, OF, and DIC methods. The effects of noise injection and downsampling on MSE were evaluated at 5% biaxial strain, with SNRs between 10 and 30 dBs and downsampling factors between 0.2 and 1 assessed.

2.3 Testing of Human Aortic Aneurysm Tissue

Patients undergoing surgery for proximal aortic aneurysms (either root or ascending aorta) were recruited. The study received ethical approval from the Health Research Authority and Regional Ethics Committee (17/NI/0160) and was sponsored by the Imperial College London Joint Research and Compliance Office, as defined under the sponsorship requirements of the Research Governance Framework (2005). Participating UK healthcare organizations conducted a rigorous process of assessing capacity and capability prior to issuing study approval. Human tissue was acquired and stored according to local guidelines in adherence to the Human Tissue Act.

Specimens were obtained *en-bloc* and acquired immediately after surgical excision in the operating theatre. Thin (~5 mm axial length) circumferential portions of the tissue were carefully dissected and immersed in formalin solution for fixation. The remainder of the aortic specimen was immersed in a 10% dimethyl sulfoxide (DMSO) in phosphate buffered saline (PBS) solution and stored within an hour in a -80 °C freezer (Bia, et al., 2006) (Figure 1).

Aortic tissue specimens were defrosted in a 4 °C refrigerator for 24 hours prior to testing. After thawing, samples were cut longitudinally and circumferentially into twelve 20 mm x 5 mm dogbone subsections, with a gauge length of 10 mm. We use "specimen" to describe the whole aortic tissue sample obtained from surgery. "Subsection" denotes a dogbone-shaped portion of the single tissue specimen, excised and used specifically in tensile testing. All subsections were tested using a TestResources USA R-Series Controller (Frame model no. 120R225; Transducer model no. SMT-1.1-294) in a 37 °C phosphate buffered saline (PBS) bath (Figure 1). The subsections were mounted lengthwise onto serrated clamps and imaged from the intimal side. A preload force of 0.01 N was used for both preconditioning and testing. Preconditioning was performed on all subsections following a similar protocol outlined in Garcia-Herrera *et al*, 2012. The subsection was cycled between 0% to 20% strain for five cycles at a crosshead speed of 2 mm/minute. After preconditioning, the subsection was tested at 2 mm/minute until sample rupture. Both the clamp displacement and force were recorded. The crosshead speed of 2 mm/minute is based off prior literature on tensile testing of aortic tissue (Sommer et. al, 2016). In total, five subsection samples were tested in this study; a comprehensive evaluation was conducted with a single aortic subsection, and four aortic subsections (two axial and two circumferential subsections) were additionally tested to assess method reproducibility.

[Figure 1 about here.]

For strain field analysis, the single-test aortic subsection was imaged using a Canon EOS 90D DSLR with a 50 mm f1.8 STM lens, and the 4 aortic subsections used in the reproducibility study were imaged using a 12 Megapixel Mako camera (Allied vision) with a fixed distortion-corrected lens. The cameras were placed 15 cm from the subsection loaded in the clamps, and images were acquired at a frequency of 0.1 Hz. The strain fields were calculated for each consecutive image pair in the sequence.

3. RESULTS

3.1 Demons Strain Tracking Algorithm and Validation Testing

The strains calculated by the Demons algorithm accurately reproduced the known strain fields in both tension and shear of an artificially strained speckle image (Figure 2). The runtime of the Demons method was 28.005 s on one active 2.9 GHz Intel i7 core for one pair of 450 × 450 16-bit greyscale images. As shown in Figure 2, for both the applied biaxial tension and shear strains, the Demons strains coincide with the unity line of the known strain fields, with slopes of 1.003 and 1.030, respectively (Table 1). In addition, the Pearson's correlation coefficient, an overall accuracy metric, was above 0.999 for both tests, indicative of a strong correlation between the calculated and known strain datasets.

While both tests were considered successful, Demons was more robust to normal than pure shear strain field assessment. The spatial standard deviations increased with strain for both tests, but the mean errors between known and derived strains were higher in the shear test, as expressed by the slightly lower Pearson's correlation coefficients shown in Table 1. For the biaxial tension test, a maximum standard deviation of 1.38% was determined in the normal direction (Table 1). In contrast, the maximal standard deviation was marginally higher in the shear direction during the shear test, at 1.83%.

[Figure 2 about here.]

[Table 1 about here]

The effects of image resolution and white noise injection were assessed on the speckle image at 5% biaxial strain (Figure 3). Overall, the Demons algorithm was robust to downsampling, though the MSE began to increase with a downsampling factor less than 0.5. Decreasing the image SNR adversely affected the MSE, particularly below 26 dB.

[Figure 3 about here.]

3.2 Validation Testing with DIC and OF Methods

The performance of Demons was superior to DIC and OF methods in estimating the strains of an artificial biaxial tension strain field applied to two aortic aneurysm tissue images (Figure 4a and b). The two images were of differing quality and assessed by PIQE scores, where lower scores indicate higher quality images; Images 1 and 2 had PIQE scores of 28.19 and 61.92, respectively. For both images, the Demons algorithm outperformed both OF and DIC in terms of spatial error between the known and calculated strain fields, as well as spatial standard deviations, at higher strain fields (Figure 4c-f). When compared to the unity line of the known strain field of Image 1, Demons had a slope of 0.986, where DIC and OF methods had slopes of 0.810 and 0.642, respectively (Table 2). Demons similarly outperformed DIC and OF methods when compared to the unity line of the known strain field of Image 2, with a slope of 0.981 achieved for the Demons algorithm, compared to 0.672 and 0.690 for DIC and OF methods, respectively. Overall, Demons achieved significantly lower maximal absolute deviations and spatial standard deviations, as well as higher Pearson's correlation coefficients, compared to OF and DIC (Table 2). Despite the lower quality of Image 2, there was only a small change in the standard deviations and Pearson's coefficients in the strain predictions from the Demons algorithm, demonstrating Demons' robustness to variation in image quality.

[Figure 4 about here]

[Table 2 about here]

Both Demons and OF outperformed DIC with respect to both noise injection and downsampling (Figure 5). Demons and OF were equally resilient to noise, performing similarly with SNR values less than 29 dB. Demons was more robust to downsampling than DIC and OF methods, up to a scale of 0.6 (310 × 310 pixels). With further downsampling, OF slightly outperformed Demons.

[Figure 5 about here]

3.3 Testing of Aortic Aneurysm Tissue

The human aortic aneurysm tissue sample was tested until failure, with rupture occurring at a recorded clamp strain of 42%, corresponding to frame 19 of 24 in Figure 6. Failure occurred in the upper portion of the sample near the clamp. The corresponding strain field maps at rupture, as determined by Demons, highlighted the location of rupture, with localized pockets of up to 95% y-normal strain observed (Figure 7). The mean normal and shear strains as determined by Demons exhibited variations due to the inhomogeneity of the arterial tissue at all strain levels, with the variations increasing near rupture. Overall, the clamp strain and the Demons y-strain approximately coincided, with mean Demons strain values being slightly higher than clamp strain (Figure 7). Recall that the Demons strain estimation is based on Green's strain, and thus differs from the engineering strain basis of clamp strain due to the additional higher order terms in the Green-Lagrange strain calculations.

[Figures 6 & 7 about here.]

After rupture, strain in the y-direction sharply decreased, which was also marked by a sharp discontinuity in the load curve. The elastic portion of the strain curve displayed hyperelastic, strain-stiffening behavior until rupture, which is common for arterial tissue. (Xiong, Wang, Zhou, & Wu, 2008) (Sokolis, Boudoulas, & Karayannacos, 2002) (Roach & Burton, 1957).

To assess the robustness of the Demons algorithm to different sample images, four additional aortic aneurysm dogbone samples were tested, with the corresponding strain assessed by Demons. As shown in Figure 8, the mean normal Demons strain in the y-direction increased monotonically with clamp strain in a manner similar to the results shown in Figure 7.

[Figure 8 about here.]

DISCUSSION

To the best of the authors' knowledge, this was the first application of a Demons-based registration algorithm to compute strain fields of deforming soft tissue undergoing tensile loading. Demons was successful in strain field computation and was able to fully capture the local dynamic behavior of aortic tissue deformation. The proposed pipeline presents a modified way of solving the Demons registration problem by simplifying the loss function and implementing an adaptive gradient descent solver, which increases the robustness of the algorithm and computational speed. When compared to other standard strain tracking methods, namely DIC and OF, the Demons algorithm outperformed both in terms of error between the known and calculated strain fields. Based on the results of this study, Demons should be applicable as a marker-less assessment of other soft tissue types. Our aortic specimens provided an appropriate test case tissue for the algorithm, since the intimal surfaces of blood vessels are generally smooth and featureless to the naked eye.

For this specific application, Demons was able to capture the evolving strain fields of aortic aneurysm tissue undergoing uniaxial tensile tests. All five samples tested demonstrated similar hyperelastic, strain-stiffening behaviors, with local strain fields that coincided with spatial points of rupture and with increasing strain filed heterogeneity. Mean normal Demons strain in the y-direction increased monotonically with clamp strain. Mean normal y-strain fields also displayed a Demons strain/clamp strain slope of approximately one at low strains, which is expected for hyperelastic materials. Deformation inhomogeneities were also captured; pockets of extreme Demons strain visually coincided with the local area of rupture.

At higher strains, the calculated Demons strain was greater than the clamp strain, the degree of which varied between the tested samples. Part of this deviation between the Demons and clamp strain is due to differing strain definitions, where Demons expression is based on Green's strain and clamp strain implements an engineering basis. However, the broad range of strain determined by Demons suggests a biomechanical contribution to this variation. It is theorized that micro-tears occur within the tissue sample at higher strains, leading to localized areas of high deformation. These are subsequently captured by the Demons algorithm, contributing to the overall increase in mean strain. This phenomenon is evident when analysing the box plots of the tested samples at higher strains; the strain range is large with a right-skewed distribution. These localized micro-tears would not impact the global behaviour of the sample recorded by tensile machine, as they would have minimal impact on the loading bearing capability of the sample, and are not reflected in the load curve as a result. These observations emphasize the inaccuracies of utilizing clamp strain to represent the strain field of soft tissues.

The large range in strain of all five samples tested raises an interesting question of how best to characterize the resulting strain field of aortic tissue when using optical strain tracking. For all samples tested, the strain distribution was right-skewed, with the mean consistently higher than the median; the degree of skewness also varied between samples due to tissue inhomogeneity. Depending on the desired objectives of a proposed study, the best metric to represent the strain field may vary. The importance of this aspect of study design is evident when analyzing the results of the Demons pipeline presented in this work.

The current runtime of the proposed method has been significantly improved via parallelization (each image pair is registered in parallel), with speeds comparable to OF and DIC. However, 85% of its run time is spent on image warping, used repetitively in calculating the vector exponential of the flow field

(Bossa, Zacur, & Olmos, 2008) and the loss function, as well as updating the flow and displacement fields. Future work could involve writing a GPU implementation to speed up the repetitive warping (Rosner, Fassold, Schallauer, & Bailer, 2010). We have achieved better performance by omitting a regularization term in the loss function, most likely because tissue micro-tearing that occurs during tensile loading violates smoothness constraints. Different regularization frameworks, dependent upon deformation behavior, should be considered.

Like many optical strain estimation algorithms, the current protocol struggled to characterize large displacements between consecutive frames, particularly compared to OF. This can be accounted for by imaging at a sufficiently high frame rate to ensure that strains between consecutive frames do not exceed 15%. While DIC also has this limitation, variational OF can correctly characterize large displacements by considering feature matching. Future work could involve utilizing spectral correspondences, such as those used in Spectral Log-Demons (Lombaert, Grady, Pennec, Ayache, & Cheriet, 2017), to include global information in the minimization scheme.

CONCLUSION

The proposed Demons algorithm generates robustly estimated strain fields from image sequences of uniaxial tensile tests of unmarked human aortic aneurysm tissue. A synthetic dataset was utilized to validate the algorithm, and real data from uniaxial tensile tests of aortic aneurysm subsections demonstrated its utility and reproducibility. The results show the efficacy of using an image-based algorithm to calculate strain fields directly from a monochromatic image sequence of aortic tissue undergoing a uniaxial tensile test. These strain measurements are particularly valuable in the assessment of aortic tissue pathologies, such as atherosclerosis, leading to better understanding of associated conditions like aortic dissection.

CONFLICT OF INTEREST STATEMENT:

All listed authors declare no conflict of interest.

ACKNOWLEDGMENTS

This research was funded by an Imperial College NIHR Biomedical Research Centre project grant.

REFERENCES

Amiot, F., Bornert, M., Doumalin, P., Dupré, J., Fazzini, M., Orteu, J., . . . Weinin, J. (2013). Assessment of Digital Image Correlation Measurement Accuracy in the Ultimate Error Regime: Main Results of a Collaborative Benchmark. *Open Archive Toulouse Archive Ouverte, 49*(6), 483-496.

Barber, B., Dobkin, D. P., & Huhdanpaa, H. (1996). The Quickhull Algorithm for Convex Hulls. *ACM Transactions on Mathematical Software*, 469-483.

Barranger, Y., Doumalin, P., Dupré, J., & Germaneau, A. (2010). Digital Image Correlation accuracy: influence of kind of speckle and recording setup. *EPJ Web of Conferenc, 6*(31002).

Bia, D., Pessana, F., Armentano, R., Perez, H., Graf, S., Zocalo, Y., . . . Alvarez, I. (2006). Cryopreservation procedure does not modify human carotid homografts mechanical properties: an isobaric and dynamic analysis. *Cell and Tissue Banking*, 183-194.

Bossa, M., Zacur, E., & Olmos, S. (2008). Algorithms for computing the group exponential of diffeomorphisms: Performance evaluation. *IEEE Computer Society Conference on Computer Vision and Pattern Recognition* , 1-8.

Boyle, J. J., Kume, M., Wyczalkowski, M. A., Taber, L. A., Pless, R. B., Xia, Y., . . . Thomopoulos, S. (2014). Simple and accurate methods for quantifying deformation, disruption, and development in biological tissues. *Journal of the Royal Society Interface, 11*(200).

Brox, T., Bregler, C., & Malik, J. (2009). Large Displacement Optical Flow. *IEEE International Conference on Computer Vision and Pattern Recognition (CVPR).*

Cahill, N., Noble, J., & Hawkes, D. (2009). A Demons algorithm for image registration with locally adaptive regularization. *Medical Image Computing and Computer-Assisted Intervention, 561,* 574-581.

Carew, E. O., Garg, A., Barber, E., & Vesely, I. (2004). Stress Relaxation Preconditioning of Porcine Aortic Valves. *Annals of Biomedical Engineering*, 563-572.

Chen, H., Zhao, X., Lu, X., & Kassab, G. (2013). Non-linear micromechanics of soft tissues. *Int J Non Linear Mech*, 79-85.

Chizat, L., & Bach, F. (2018). On the Global Convergence of Gradient Descent for Over-parameterized Models using Optimal Transport. *arXiv*.

Choudhury, N., Bouchot, O., Rouleau, L., Tremblay, D., Cartier, R., Butany, J., . . . Leask, R. (2009). Local mechanical and structural properties of healthy and diseased human ascending aorta tissue. *Cardiovascular Pathology*, 83-91.

Danpinid, A., Luo, J., Vappou, J., Terdtoon, P., & Konofagou, E. E. (2010). In Vivo Characterization of the Aortic Wall Stress-Strain Relationship. *Ultrasonics , 50*(7), 654-665.

Duprey, A., Khanafer, K., Schlicht, M., Avril, S., Williams, D., & Berguer , R. (2010). In VitroCharacterisation of Physiological andMaximum Elastic Modulus of Ascending ThoracicAortic Aneurysms Using Uniaxial Tensile Testing. *European Journal of Vascular and Endovascular Surgery*, 700-707.

Hiorns, J., Bidan, C., Jensen, O., Gosens, R., Kistemaker, L. E., Fredberg, J. J., . . . Brook, B. S. (2016). Airway and Parenchymal Strains during Bronchoconstriction in the Precision Cut Lung Slice. *Fronteirs in Physiology*, *7*(309).

Huang, L., Korhonen, R., Turunen, M., & Finnila, M. (2019). Experimental mechanical strain measurement of tissues. *PeerJ*.

Khanafer, K., Duprey, A., Zainal, M., Schlicht, M., Williams, D., & Berguer, R. (2011). Determination of the elastic modulus of ascending thoracic aortic aneurysm at different ranges of pressure using uniaxial tensile testing. *The Journal of Thoracic and Cardiovascular Surgery*, 682-686.

Kim, J., Badel, P., Duprey, A., Favre, J., & Avril, S. (2011). Characterisation of failure in human aortic tissue using digital image correlation. *Computer Methods in Biomechanics and Biomedical Engineering*, *14*(sup1), 73-74.

Lionello, G., & Cristofolini, L. (2014). A practical approach to optimizing the preparation of speckle patterns for digital-image correlation. *Measurement Science and Technology*, *25*(10).

Lionello, G., & Cristofolini, L. (2014). A practical approach to optimizing the preparation of speckle patterns for digital-image correlation. *Measurement Science and Technology*, *25*(10).

Lombaert, H., Grady, L., Pennec, X., Ayache, N., & Cheriet, F. (2017). Spectral Log-Demons: Diffeomorphic Image Registration with Very Large Deformations. *International Journal of Computer Vision, Springer Verlag, 107*(3), 254-271.

Loshchilov, I., & Hutter, F. (2017). SGDR: Stochastic Gradient Descent with Warn Restarts. *ICLR*.

Olufsen, S., & Andersen, M. E. (2019). *μDIC: A Python toolkit for Digital Image Correlation (DIC) CircleCI codecov Documentation Status*. Retrieved September 2019, from https://pypi.org/project/muDIC/

Palanca, M., Tozzi, G., & Cristofolini, L. (2016). The use of digital image correlation in the biomechanical area: a review. *International Biomechanics*, 1-21.

Pan, B., Qian, K., Xie, H., & Asundi, A. (2009). Two-dimensional digital image correlation for in-plane displacement and strain measurement: a review. *Measurement Science and Technology*.

Roach, M. R., & Burton, A. C. (1957). The Reason for the Shape of the Distensibility Curves of Arteries. *Canadian Journal of Biochemistry and Physiology*, 681-690.

Rosner, J., Fassold, H., Schallauer, P., & Bailer, W. (2010). Fast GPU-based image warping and inpainting for frame interpolation. *Proceedings of Computer Graphics, Computer Vision and Mathematics*.

Silver, F. H., & Shah, R. (2016). Measurement of mechanical properties of natural and engineered implants. *Tissue Engineering & Regenerative Medicine, 1*(1), 20-25.

Sokolis, D., Boudoulas, H., & Karayannacos, P. (2002). Assessment of the aortic stress-strain relation in uniaxial tension. *Journal of Biomechanics, 35*(9), 1213-1223.

Thirion, J.-P. (1998). Image matching as a diffusion process: an analogy with Maxwell's demons. *Medical Image Analysis, 2*(3), 243-260.

Vercauteren, T., Pennec, X., Perchant, A., & Ayache, N. (2009). Diffeomorphic Demons: Efficient Non-parametric Image Registration. *NeuroImage, 45*(1), S61-72.

Vorp, D. (2007). Biomechanics of abdominal aortic aneurysm. *Journal of Biomechanics* , 1887-1902.

Watton, P., & Hill, N. (2007). Evolving mechanical properties of a model of abdominal aortic aneurysm. *Biomechanics and Modeling in Mechanobiology, 8*(1), 25-42.

Xiong, J., Wang, S., Zhou, W., & Wu, J. (2008). Measurement and analysis of ultimate mechanical properties, stress-strain curve fit, and elastic modulus formula of human abdominal aortic aneurysm and nonaneurysmal abdominal aorta. *Journal of Vascular Surgery*, 189-195.

LIST OF FIGURES

1 Explanted human aortic sample (**A** - left). Dogbone-shaped subsection (**A** - middle) are cut out for mechanical testing. An image of a portion of a dogbone subsection (**A** - right) was used for validation. (**B)** shows the test rig used for uniaxial tensile loading. Aortic subsections were attached with serrated clamps. Clamp strain was recorded continuously, and images were captured every 10 seconds.

2 An artificial biaxial strain field (maximum 50% strain) was applied on a speckled image (**A**) for 50 frames, and strains were assessed using the Demons algorithm (**C**). Similarly, an artificial shear strain field (maximum 50% strain) was applied on the speckled image (**B**) for 50 frames, and strains were calculated (**D**). Red arrows indicate directionality of strain fields in (**A)** and (**B)**. Average of the normal strain components are calculated as $\frac{1}{num\_pixels}\left\{\sum_{pixels}\frac{E_{xx}+E_{yy}}{2}\right\}$ and the average shear strain components are calculated as $\frac{1}{num\_pixels}\left\{\sum_{pixels} E_{xy}\right\}$.

T1 Maximal deviation, maximal standard deviation, Pearson's Correlation coefficients, and best-fit slopes (regression coefficients) of normal and shear strain fields calculated with the Demons algorithm for up to 50% biaxial and shear strain applied to a speckle image.

3 Log-scale mean-squared error vs. downsampling factor (**A**) and signal-to-noise ratio (**B**) were analyzed for a 5% biaxial strain field on the speckle image.

4 Comparison of performance of Demons, OF, and DIC on the two aortic subsample images undergoing artificial biaxial strain. Image 1 with a low PIQE score is displayed in (**A)**, and Image 2 with a high PIQE score is displayed in (**B)**. (**C)** and (**D)** display mean calculated horizontal strains of the three algorithms for Images 1 and 2 respectively. (**E)** and (**F)** display mean calculated shear strains of the three algorithms for Images 1 and 2 respectively. Error bars represent 1 standard deviation for all plots.

T2 Maximal deviation, maximal standard deviation, and Pearson's Correlation coefficients, and best-fit slopes (regression coefficients) of normal and shear strain fields calculated with Demons, OF, and DIC for up to 50% biaxial and shear strain applied to the two aortic images in Figures 5A and B.

5 Log-scale mean-squared error vs. downsampling factor (**A**), and noise (**B**) for aortic image 1 (Figure 4A). OF shows higher robustness to lower resolutions (higher downsampling) than both Demons and DIC, however demons outperform both OF and DIC at higher resolutions. Demons and OF show comparable robustness and accuracy to noise injection.

6 Uniaxial tensile test of a human aortic tissue subsection. Visible rupture occurs in the 19th frame, where there was a sharp decrease in tension. The region of interest (ROI) (highlighted in yellow in frame 19) for strain-field analysis is confined to the maximal area of the image with only tissue present (absent of any background) before tearing. The area of initiation of tearing is indicated by the green arrow.

7 Strain tracking was applied to an ROI (Figure 1A) of the aortic tissue subsection in Figure 7, which undergoes tensile loading until rupture. The strain fields of the ROI at rupture (determined from the decrease in tension to occur at frame 19, clamp strain 42%) are shown at left, with the green arrow indicating visible evidence of the point of rupture. Plots of x strain (top right), applied load and y- strain (middle right), and shear strain (bottom right) include box plots showing the 25th percentile, median, 75th percentile, and range of the strain components, accompanied by the mean strain values (continuous blue curves). The nonlinearity of the force curve is due to strain-stiffening, a well-observed behavior in arterial tissue. Variations in strain field are mainly due to tissue inhomogeneities.

8 Strain tracking was applied to 4 different subsections from one chosen patient case (Subsection 1-4), with the same plot formats and parameters as in Figure 10. Strain measurements are shown up to the point of rupture.

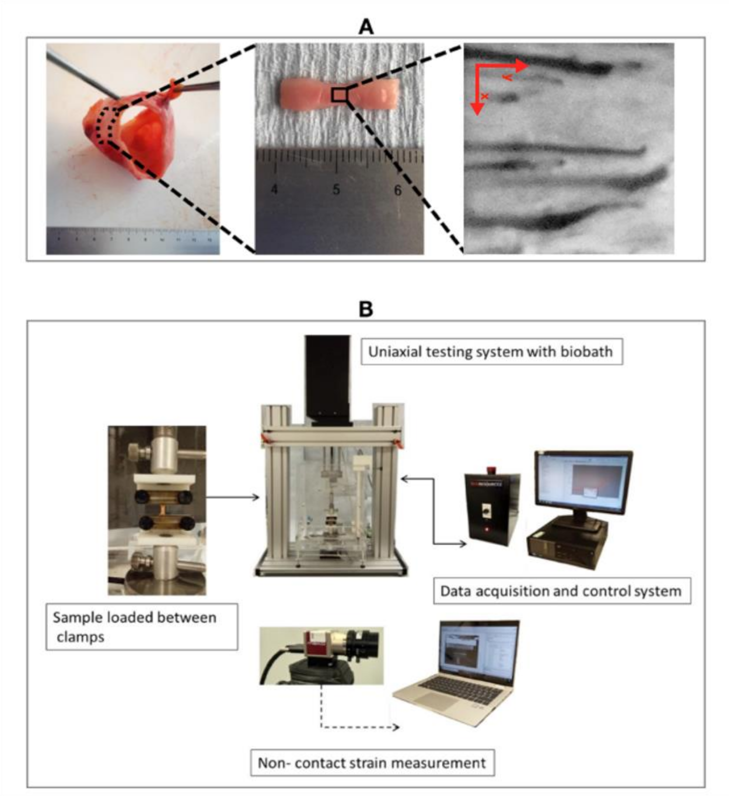

Figure 1. Explanted human aortic sample (**A** - left). Dogbone-shaped subsection (**A** - middle) are cut out for mechanical testing. An image of a portion of a dogbone subsection (**A** - right) was used for validation. (**B)** shows the test rig used for uniaxial tensile loading. Aortic subsections were attached with serrated clamps. Clamp strain was recorded continuously, and images were captured every 10 seconds.

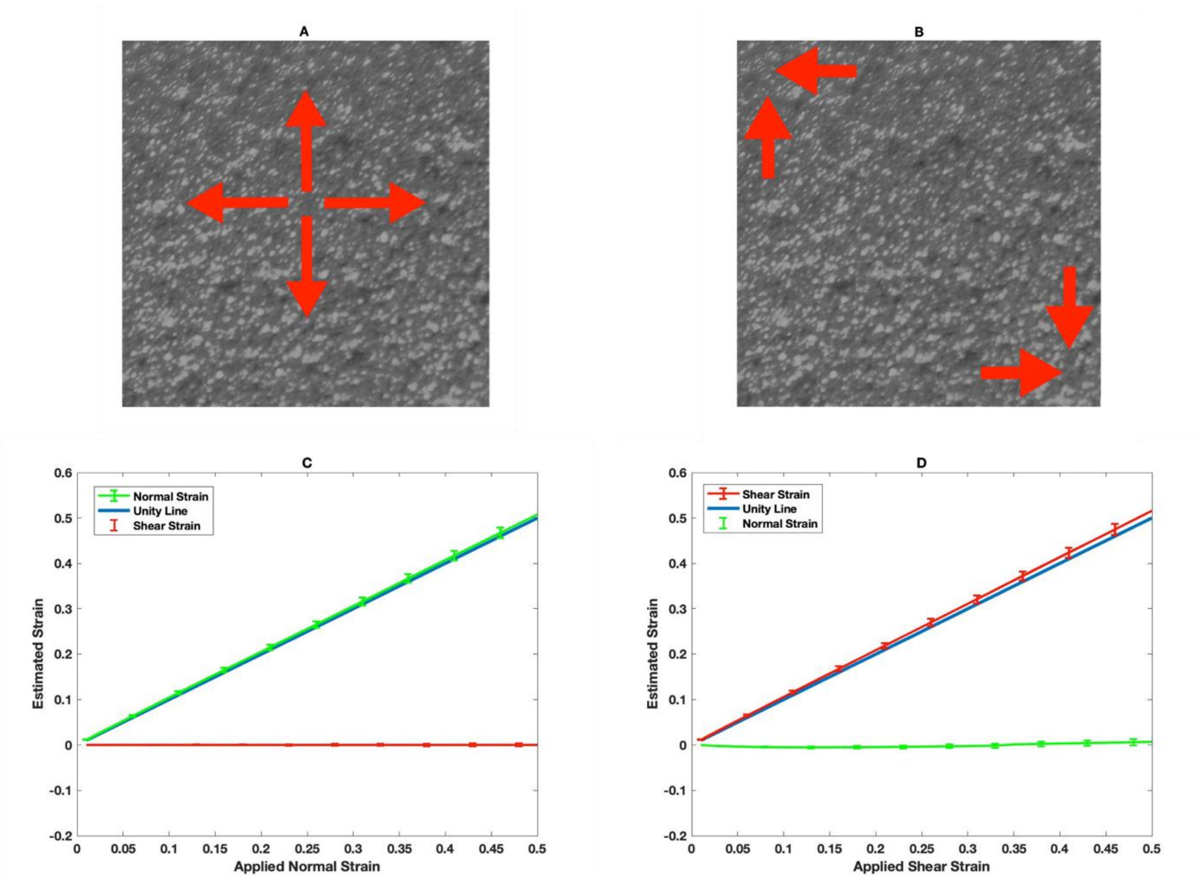

Figure 2. An artificial biaxial strain field (maximum 50% strain) was applied on a speckled image (**A**) for 50 frames, and strains were assessed using the Demons algorithm (**C**). Similarly, an artificial shear strain field (maximum 50% strain) was applied on the speckled image (**B**) for 50 frames, and strains were calculated (**D**). Red arrows indicate directionality of strain fields in (**A)** and (**B)**. Average of the normal strain components are calculated as $\frac{1}{num\_pixels}\left\{\sum_{pixels}\frac{E_{xx}+E_{yy}}{2}\right\}$ and the average shear strain components are calculated as $\frac{1}{num\_pixels}\{\sum_{pixels} E_{xy}\}$.

Figure

Click here to access/download;Figure;Figure_3.docx

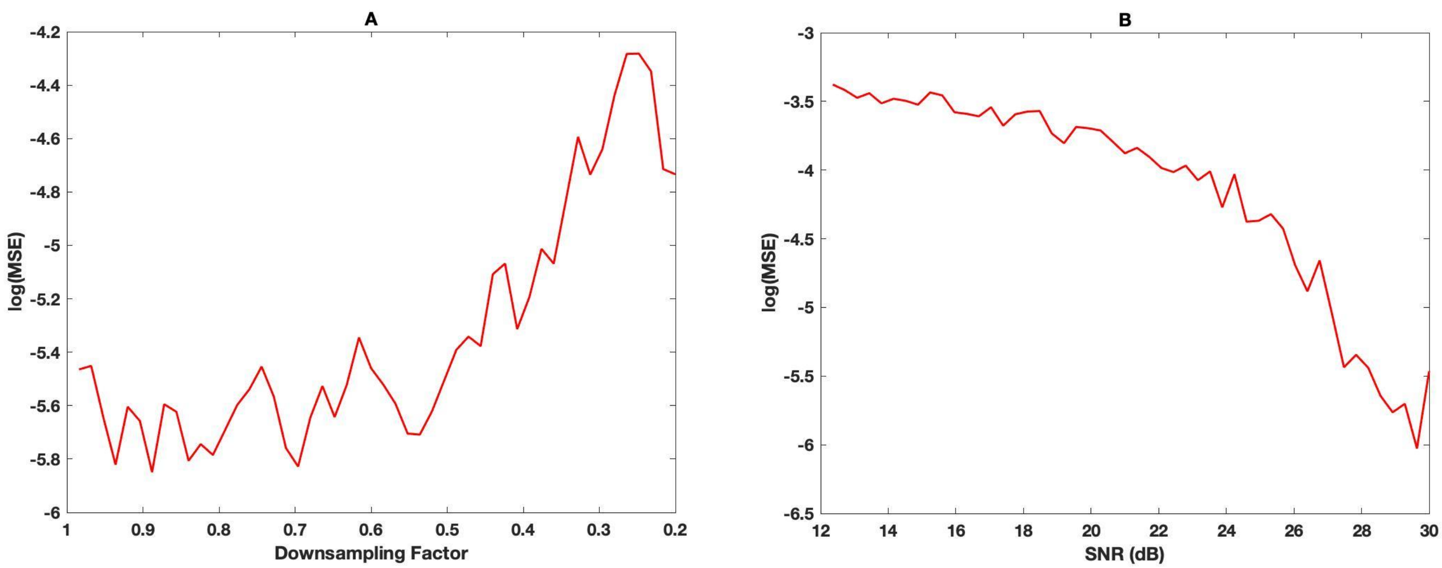

Figure 3. Log-scale mean-squared error vs. downsampling factor (**A**) and signal-to-noise ratio (**B**) were analyzed for a 5% biaxial strain field on the speckle image.

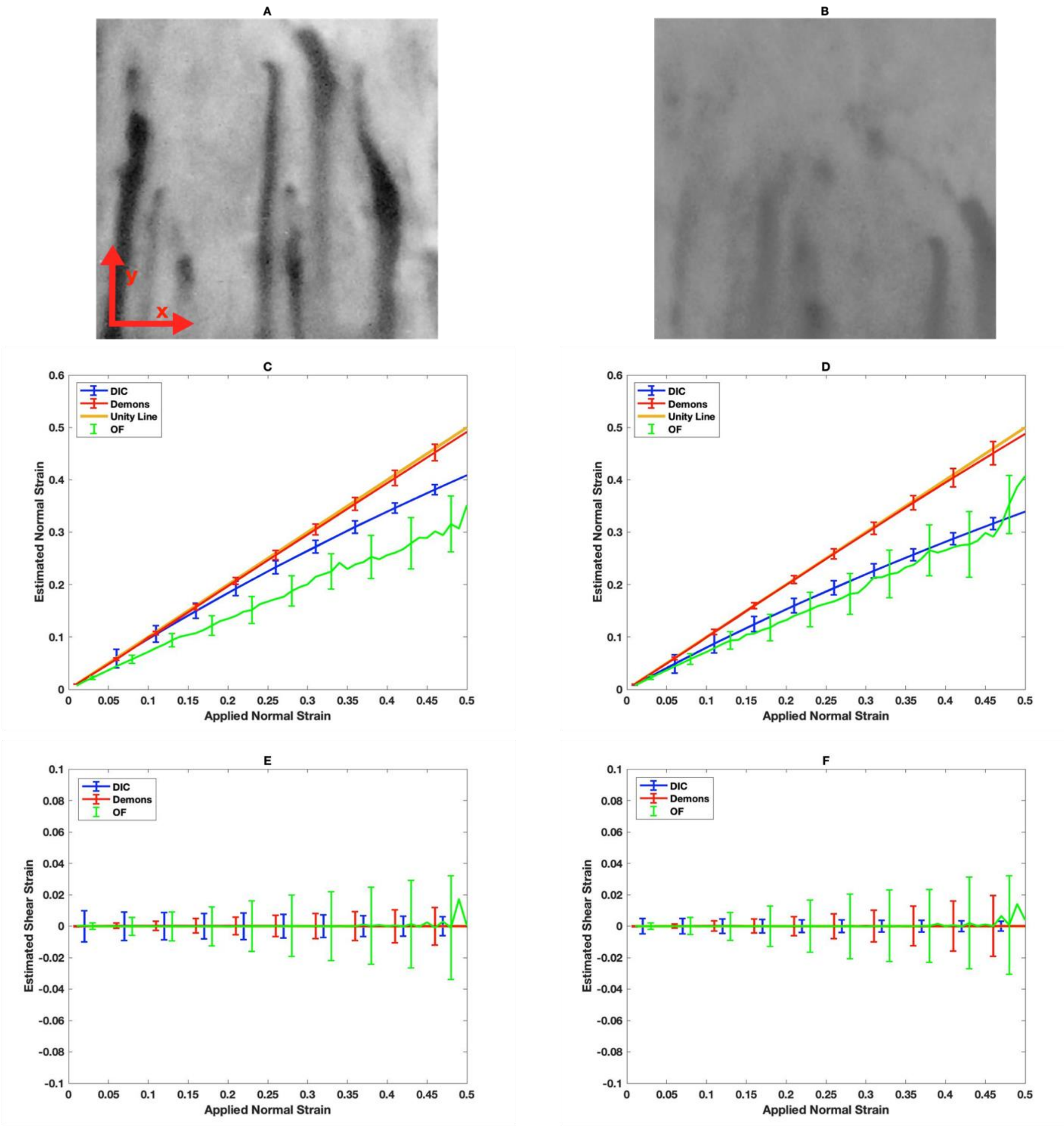

Figure 4. Comparison of performance of Demons, OF, and DIC on the two aortic subsample images undergoing artificial biaxial strain. Image 1 with a low PIQE score is displayed in (**A**), and Image 2 with a high PIQE score is displayed in (**B**). (**C)** and (**D)** display mean calculated horizontal strains of the three algorithms for Images 1 and 2 respectively. (**E)** and (**F)** display mean calculated shear strains of the three algorithms for Images 1 and 2 respectively. Error bars represent 1 standard deviation for all plots.

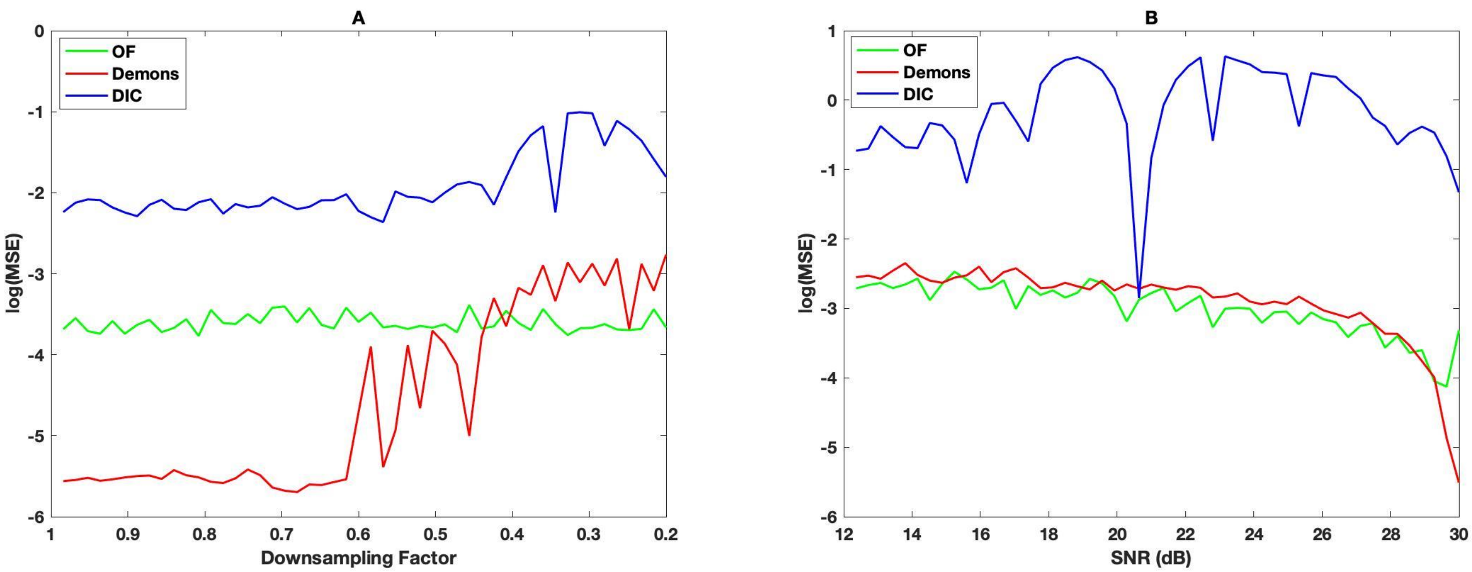

Figure 5. Log-scale mean-squared error vs. downsampling factor (**A**), and noise (**B**) for aortic image 1 (Figure 4A). OF shows higher robustness to lower resolutions (higher downsampling) than both Demons and DIC, however demons outperform both OF and DIC at higher resolutions. Demons and OF show comparable robustness and accuracy to noise injection.

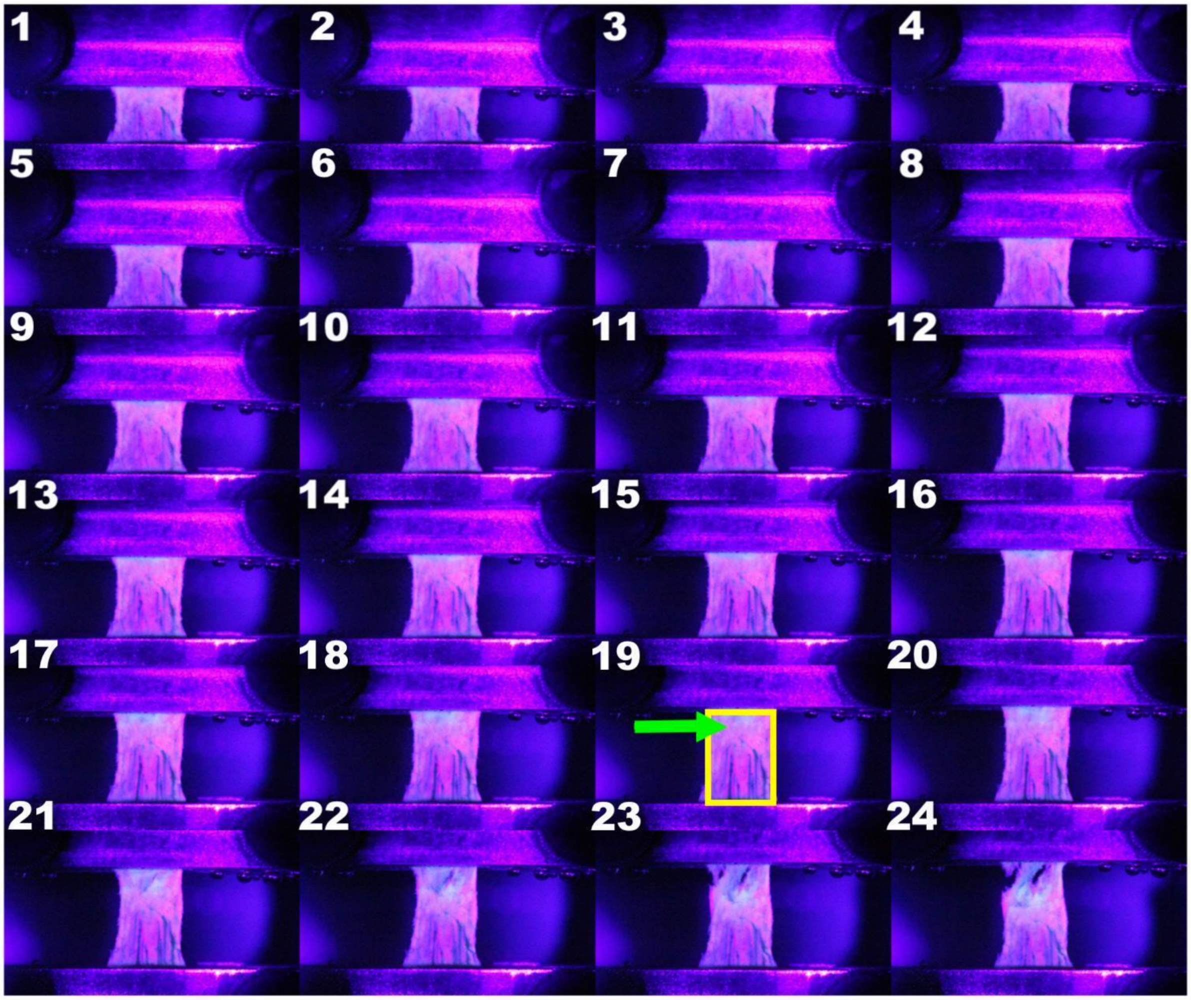

Figure 6. Uniaxial tensile test of a human aortic tissue subsection. Visible rupture occurs in the 19th frame, where there was a sharp decrease in tension. The region of interest (ROI) (highlighted in yellow in frame 19) for strain-field analysis is confined to the maximal area of the image with only tissue present (absent of any background) before tearing. The area of initiation of tearing is indicated by the green arrow.

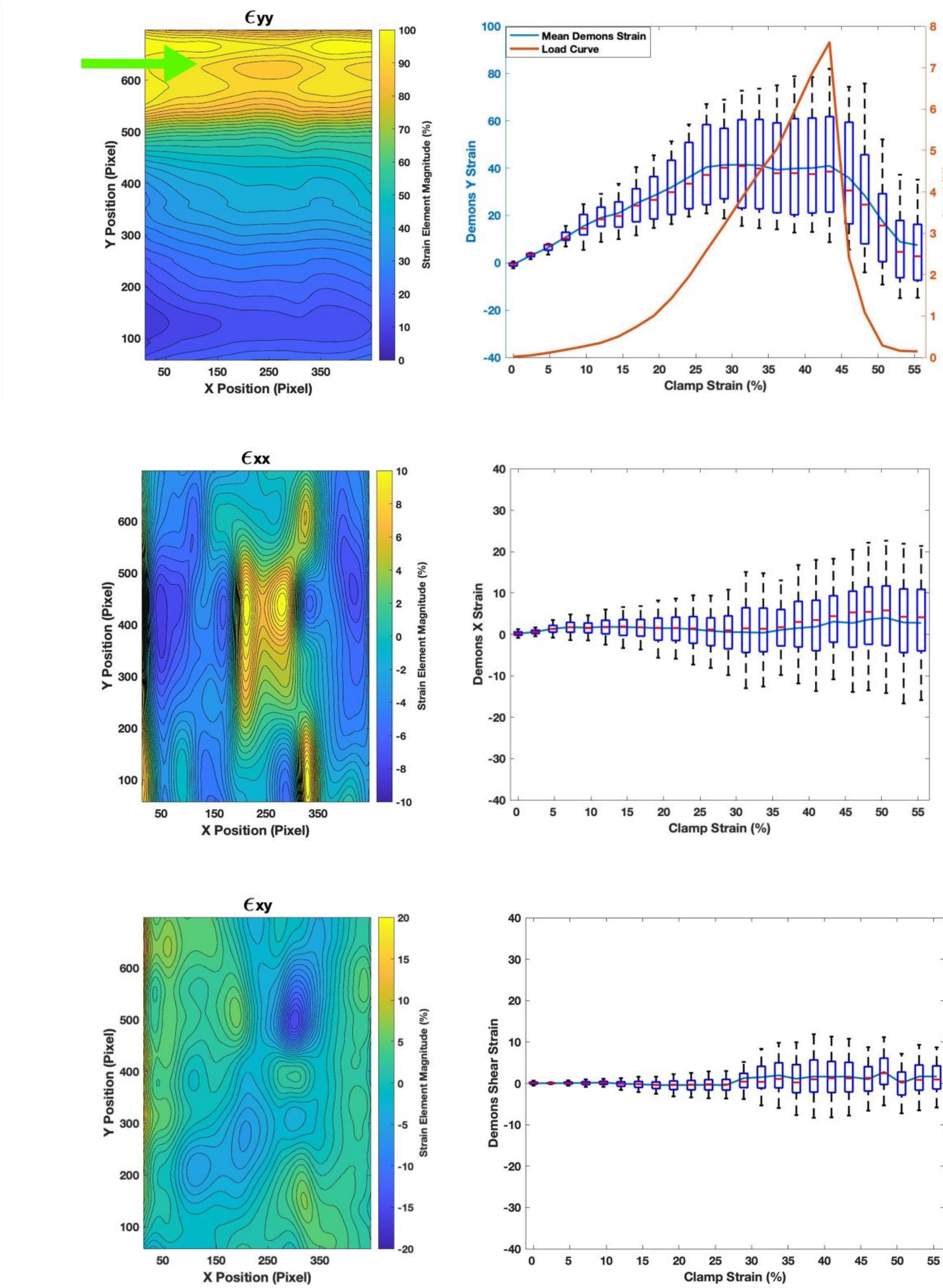

Figure 7. Strain tracking was applied to an ROI (Figure 1A) of the aortic tissue subsection in Figure 7, which undergoes tensile loading until rupture. The strain fields of the ROI at rupture (determined from the decrease in tension to occur at frame 19, clamp strain 42%) are shown at left, with the green arrow indicating visible evidence of the point of rupture. Plots of x strain (top right), applied load and y- strain (middle right), and shear strain (bottom right) include box plots showing the 25th percentile, median, 75th percentile, and range of the strain components, accompanied by the mean strain values (continuous blue curves). The nonlinearity of the force curve is due to strain-stiffening, a well-observed behavior in arterial tissue. Variations in strain field are mainly due to tissue inhomogeneities.

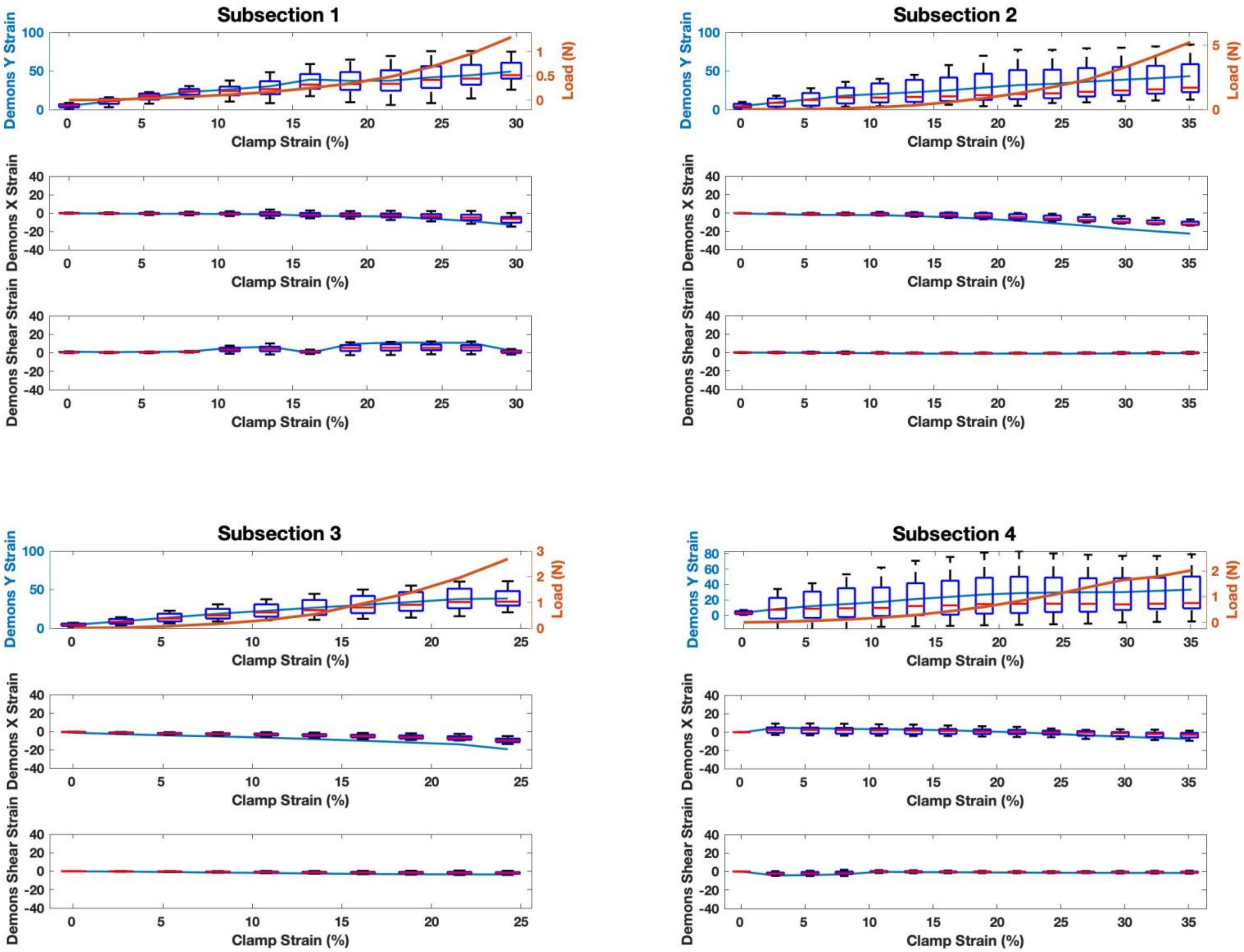

Figure 8. Strain tracking was applied to 4 different subsections from one chosen patient case (Subsection 1-4), with the same plot formats and parameters as in Figure 10. Strain measurements are shown up to the point of rupture.

Speckle Image															
Biaxial Test								Shear Test							
Normal				Shear				Shear				Normal			
Max Dev. (%)	Max SD (%)	P Coeff.	Reg Coeff.	Max Dev. (%)	Max SD (%)	P Coeff.	Reg Coeff.	Max Dev. (%)	Max SD (%)	P Coeff.	Reg Coeff.	Max Dev. (%)	Max SD (%)	P Coeff.	Reg Coeff.
0.64	1.38	0.9996	1.0027	0.10	0.15	0.9999	-1.19e-6	1.33	1.83	0.9990	1.0296	0.17	0.45	0.9996	-0.0032

Table 1. Maximal deviation, maximal standard deviation, Pearson's Correlation coefficients, and best-fit slopes (regression coefficients) of normal and shear strain fields calculated with the Demons algorithm for up to 50% biaxial and shear strain applied to a speckle image.

	Aortic Image 1 (Figure 5A)							
	Normal				Shear			
	Max Dev. (%)	Max SD (%)	P Coeff.	Reg Coeff.	Max Dev. (%)	Max SD (%)	P Coeff.	Reg Coeff.
Demons	1.71	1.59	0.9981	0.986	0.85	1.33	0.9997	-4.28e-5
OF	17.48	6.86	0.9850	0.641	1.87	4.18	0.9938	0.005
DIC	9.34	1.80	0.9932	0.809	0.04	1.82	0.9999	-7.05e-6

	Aortic Image 2 (Figure 5B)							
	Shear				Normal			
	Max Dev. (%)	Max SD (%)	P Coeff.	Reg Coeff.	Max Dev. (%)	Max SD (%)	P Coeff.	Reg Coeff.
Demons	2.80	3.25	0.9963	-8.42e-6	0.09	2.11	0.9997	0.9809
OF	13.85	7.23	0.9618	0.0064	1.44	3.90	0.9971	0.6897
DIC	15.29	1.96	0.9903	-1.18e-6	0.07	0.17	0.9999	0.6721

Table 2. Maximal deviation, maximal standard deviation, and Pearson's Correlation coefficients, and best-fit slopes (regression coefficients) of normal and shear strain fields calculated with Demons, OF, and DIC for up to 50% biaxial and shear strain applied to the two aortic images in Figures 5A and B.

CONFLICT OF INTEREST STATEMENT

All listed authors declare no conflict of interest.

Mark D. Olchanyi

Amir Sadikov

Sumesh Sasidharan

M Yousuf Salmasi

Lowell T. Edgar

Jennifer Frattolin

Omar Jarral

Thanos Athanasiou

James E. Moore Jr